

Electroabsorption spectroscopy of Ge/Si self-assembled islands

M. El kurdi, P. Boucaud,^{a)} S. Sauvage, F. Aniel, and G. Fishman

Institut d'Électronique Fondamentale, Unité Mixte de Recherche (UMR) Centre National de la Recherche Scientifique (CNRS) 8622, Bâtiment 220, Université Paris-Sud, 91405 Orsay, France

O. Kermarrec, Y. Campidelli, and D. Bensahel

STMicroelectronics, 850 Rue Jean Monnet, 38926 Crolles Cedex, France

G. Saint-Girons, I. Sagnes, and G. Patriarche

Laboratoire de Photonique et Nanostructures, Route de Nozay, 91406 Marcoussis, France

(Received 22 September 2003; accepted 26 January 2005; published online 6 April 2005)

We have performed an electroabsorption spectroscopy of Ge/Si self-assembled islands *simultaneously* in the near-infrared and in the midinfrared spectral range. The investigated structure consists of self-assembled Ge/Si islands embedded in a *p-i-n* junction. This active region is inserted into a 3- μm -thick $\text{Si}_{0.98}\text{Ge}_{0.02}$ waveguiding layer. Under a positive applied bias, the injected carriers give rise to a current-induced absorption resonant at 185 meV along with an enhanced transmission around 800 meV. The 185-meV resonance is polarized along the growth axis of the islands. The assignment of the optical transitions is made on the basis of a 14-band quantum well $\mathbf{k}\cdot\mathbf{p}$ calculation. We show that the midinfrared electroabsorption of the islands is associated with a bound-to-continuum transition between the ground states and the wetting layer states. The enhancement of the transmission is correlated to the bleaching of the interband absorption which results from hole injection in the islands. The carrier density and the parameters governing the carrier dynamics in the islands are deduced from the midinfrared modulation amplitude. An Auger recombination coefficient in the islands, $C=1.6\times 10^{-30}\text{ cm}^6\text{ s}^{-1}$, is deduced at room temperature.

© 2005 American Institute of Physics. [DOI: 10.1063/1.1874296]

I. INTRODUCTION

Self-assembled islands can be epitaxially grown by depositing pure Ge layers on a silicon substrate.¹ The Stranski–Krastanow growth mode leads to the formation of islands with different sizes and shapes including pyramidal and dome-shaped geometries.² After silicon capping, the islands sitting above a two-dimensional wetting layer exhibit a rich Ge composition.^{3,4} This large Ge content leads to two distinct features: (i) the islands are characterized by optically active transitions both in absorption and emission in the near-infrared spectral range around 1.5 μm ,⁵ and (ii) a large band offset appears in the valence band between the islands and the silicon barrier thus allowing the observation of intraband transitions in the midinfrared spectral range.^{6,7} These interband and intraband optical transitions of Ge/Si islands can be used for the development of optoelectronic or photonic devices that can operate in the near-infrared and in the midinfrared spectral range. Meanwhile the careful analysis of these optical transitions and their polarization selection rules can provide valuable information on the carrier confinement in the islands and on the carrier dynamics. These informations can be obtained by using structures under optical or electrical carrier injection.^{8,9}

In this article, we investigate *simultaneously* both interband and intraband optical processes in Ge/Si self-assembled islands by electroabsorption spectroscopy. The electroabsorption experiments are performed in a waveguide geom-

etry. In the near-infrared spectral range, the carrier injection leads to an enhanced transmission associated with the bleaching of the interband absorption. In the midinfrared spectral range, the electroabsorption is characterized by a resonant absorption around 185 meV that is polarized along the growth axis of the islands. We show that the optical properties of the islands can be described by a 14-band quantum well $\mathbf{k}\cdot\mathbf{p}$ calculation. The 185-meV resonance is associated with a bound-to-continuum intraband transition between the island's lowest lying states and the continuum of states of the wetting layer subband. The amplitude of this current-induced absorption as a function of the current density allows the measurement of the extrinsic and Auger-related recombination rates in the islands. We show that the carrier density in the Ge/Si islands is limited by Auger-related recombination mechanisms at high current densities and we provide a measurement of the Auger recombination coefficient at room temperature.

The article is organized as follows. The experimental details are given in Sec. II. The current-induced modulation of the interband and intraband absorptions are described in Sec. III. Section IV discusses the origin of the absorption, as deduced from a 14-band $\mathbf{k}\cdot\mathbf{p}$ calculation. The carrier density and the capture time of the carriers is finally discussed in Sec. V.

II. EXPERIMENTAL DETAILS

The investigated sample was grown by chemical-vapor deposition on a 200-mm Si (001)-oriented substrate.¹⁰ The deposition temperature was 700 °C and the total pressure

^{a)}Electronic mail: philippe.boucaud@ief.u-psud.fr

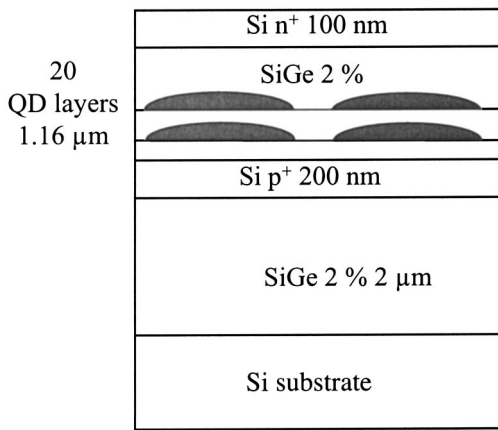


FIG. 1. Schematic diagram of the investigated sample.

was around 100 Torr. Silane and germane diluted in hydrogen were used as gas precursors. Pure germanium was deposited to induce the nucleation of the self-assembled islands. The self-assembled layers were grown in a *p-i-n* junction embedded in a midinfrared waveguide. Figure 1 shows a schematic diagram of the investigated sample. It consists of a 2- μm -thick $\text{Si}_{0.98}\text{Ge}_{0.02}$ layer, a 200-nm-thick p^+ layer (10^{19} cm^{-3}), an 80-nm-thick $\text{Si}_{0.98}\text{Ge}_{0.02}$ spacer layer, 20 self-assembled layers separated by 50-nm-thick $\text{Si}_{0.98}\text{Ge}_{0.02}$ spacer layers, an 80-nm-thick $\text{Si}_{0.98}\text{Ge}_{0.02}$ spacer layer, and a 100-nm-thick n^+ (10^{19} cm^{-3}) silicon layer. The spacer layers and the self-assembled layers are nominally undoped. The $\text{Si}_{0.98}\text{Ge}_{0.02}$ layer, with a refractive index difference of 6×10^{-3} as compared to silicon, allows the waveguiding of the light injected through the cleaved facet.¹¹ The samples were processed into ridge waveguides with a width of 100 μm and a length of 4 mm. Ohmic contacts were obtained by depositing Ti/Au alloys. The electroabsorption measurements were performed at room temperature using a step-scan Fourier-transform infrared spectrometer coupled to an infrared microscope. The spectrometer can be used either with a glow bar source and a midinfrared beam splitter or with a halogen lamp and a near-infrared beam splitter. The light was coupled and collected into the waveguide with the $\times 15$ Cassegrain optics of the microscope. The sample was either forward or reverse biased at a frequency of 5 kHz. The modulated transmission of the sample was filtered with a lock-in amplifier before the Fourier transform.

A cross-section transmission electron microscopy image of the first layers of the islands is reported in Ref. 12. A vertical correlation between the successive layers is observed because of the strain field of the buried layers. Separate images show that an oblique stacking occurs for some island columns after the deposition of multiple layers.¹³ The thickness of the silicon capping layer is not sufficient to flatten the surface above a deposited layer, thus leading to an undulated growth. While the islands in the first layers exhibit a dome-shaped geometry, the geometry of the upper layers evolves into a “boomerang” shape. The typical island height is around 20 nm and the lateral size of the first layers is around 80 nm. We note that since the island height is large, the quantum confinement along the z growth axis and its fluctuation associated with the vertical inhomogeneity in the island stack remains weak. The island density is around $3 \times 10^9 \text{ cm}^{-2}$, as estimated from separate atomic force microscopy measurements. A key feature characterizing the buried islands is their Ge content and their strain distribution. These parameters depend obviously on the deposition processes and on the capping procedure. It has been shown that a high growth temperature enhances the intermixing of uncapped islands deposited by chemical-vapor deposition.¹⁴ Interdiffusion induced by a strain-driven alloying mechanism exists even for freestanding Ge/Si islands.¹⁵ The capping of the islands by silicon leads to a significant material and strain redistribution.^{3,4} We have shown in a previous publication that the Ge content of buried islands grown at 650 and 550 $^\circ\text{C}$ by chemical-vapor deposition was around 50%.³ In the following, we will consider a 50% Ge content as a characteristic value for the buried islands and we assume in the calculation a tetragonal distortion of the SiGe alloy. Photoluminescence of Ge islands with a 50% Ge content is expected to be maximum around 0.8 eV,¹⁶ as experimentally observed.

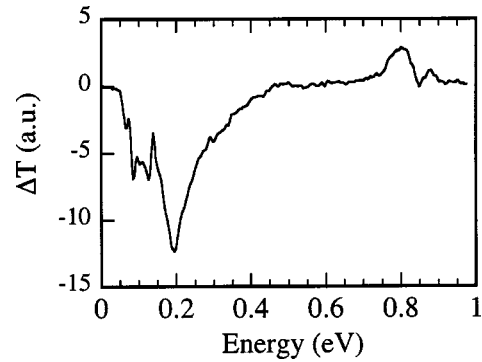


FIG. 2. Room-temperature current-induced transmission modulation. The injected current density is 17.5 A cm^{-2} . The spectrum is not normalized by the response of the optical system. Two resonances with opposite signs are observed around 200 and 800 meV. They correspond to an absorption and to an increase of transmission, respectively.

III. CURRENT-INDUCED MODULATION OF THE INTERBAND AND INTRABAND ABSORPTIONS

Figure 2 shows a typical current-induced absorption spectrum measured at room temperature under a forward applied bias. The signal-to-noise ratio is weak at high energy because of the cutoff of the midinfrared beam splitter, glow bar source, and detector. The spectrum is not corrected for the spectral response of the source, beam splitter, and detector. Only the phase correction recorded for the background spectrum without the sample is used. The simultaneous measurement of the electromodulation in the midinfrared and in the near-infrared spectral range highlights two distinct features. Two resonances with opposite signs can be observed at 185 and 800 meV. The low-energy resonance at 185 meV is associated with a decrease of transmission while the high-energy resonance corresponds to an increase of transmission. As will be shown below, these resonances correspond to both intraband and interband optical processes.

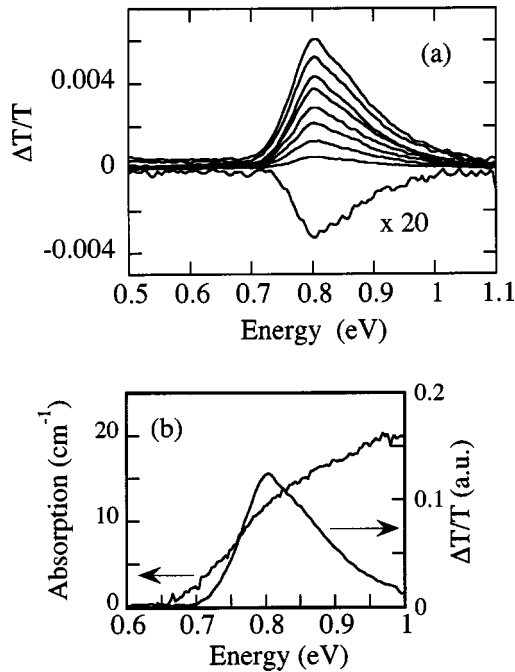


FIG. 3. (a) Near-infrared variation transmission for different injected carrier densities. From bottom to top, the injected current is 0.37, 1.5, 3.5, 5.2, 9.5, 12.7, 17.5, and 23.5 A cm⁻². The curve with an opposite sign corresponds to a reverse applied bias of 3.4 V. The amplitude in reverse bias has been multiplied by a factor of 20. (b) Comparison between the electromodulation and the interband absorption.

The spectral dependence of the near-infrared resonance as a function of the injected current is shown in Fig. 3(a). The spectra are normalized by the transmission of the source through the sample. Under a reverse applied bias, the electromodulated signal corresponds to an absorption while under a forward applied bias, the electromodulated signal corresponds to an increase of transmission, i.e., a bleaching of the absorption. The increased transmission has an onset around 0.7 eV with a maximum around 0.8 eV and a broadening (full width at half maximum) of 150 meV. Figure 3(b) shows a comparison between the electromodulation and the interband absorption measured with the same sample.¹⁰ The onset of the absorption is close to the onset of the electromodulation. We thus associate this electromodulation with the self-assembled islands. The amplitude of the modulation depends on the carrier filling of the islands. No broadening or spectral shift of the resonance is observed as the current density increases. The amplitude of the absorption modulation is much weaker in reverse bias as compared to in forward bias and rapidly saturates. The increase of absorption at reverse applied bias indicates the existence of a residual *p* doping in the islands, the reverse applied bias leading to hole depletion.⁹ Under forward bias, the absorption modulation reaches 0.6% at 1.5 μm after a 4-mm propagation through the waveguide.

Figure 4 shows the electroabsorption in the midinfrared spectral range as a function of the current density. A strong resonance superimposed on a monotonously increasing background towards low energy is observed at 185 meV. The resonance has a linewidth of 50 meV. No spectral shift and broadening of the resonance are observed as the current den-

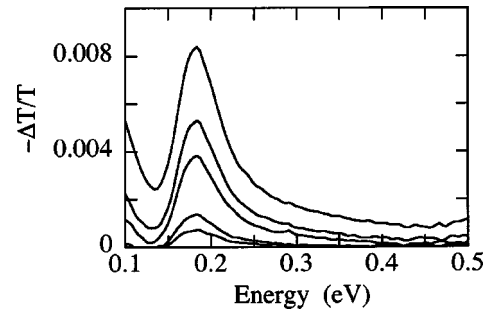


FIG. 4. Electroabsorption in the midinfrared spectral range as a function of the current density. The infrared light is unpolarized. From bottom to top, the injected current density is 0.75, 1.75, 6.5, 11, and 21 A cm⁻².

sity increases. As observed for the interband absorption, a reverse applied bias leads to hole depletion in the islands and thus to an increase of the transmission (not shown). The resonance energy of 185 meV corresponds to the energy difference between the no-phonon radiative recombination of the wetting layer (1 eV at low temperature) and the energy of the photoluminescence of the self-assembled islands (810 meV at resonance at low temperature).¹⁰ This resonance is thus attributed to the hole intraband absorption between the island's lowest lying ground states to the wetting layer sub-band. Note that the photoluminescence measurements were performed at low temperature. The energy difference between the wetting layer and the island ground state is not expected to vary significantly with temperature. This assignment is further supported by the 14-band **k**·**p** calculation presented below. The absorption is strongly transverse-magnetic (TM) polarized, i.e., the polarization of the absorption is along the growth axis.¹² This strong TM polarization is consistent with a charge displacement along the *z* growth axis from islands to wetting layers. The resonant absorption amplitude obtained after propagation along the 4-mm waveguide and after base line subtraction reaches 1.2% in TM polarization for a 21 A cm⁻² current density. We note that we can rule out transitions from the wetting layer states to be at the origin of the 185-meV resonance since the population of the wetting layers at room temperature is not significant as compared to the population of the islands.

IV. ORIGIN OF THE ABSORPTION

The height of the self-assembled islands is much smaller than their lateral dimensions. A first estimation of their electronic structure can be obtained by only considering the confinement along the *z* direction, i.e., neglecting the confinement in the layer plane. We have thus modeled the eigenstates and the infrared absorption of the islands in the framework of a 14-band quantum well **k**·**p** theory. This formalism accounts for the Γ_7^+ and Γ_8^+ valence bands and for the Γ_6^- , Γ_8^- (*p*-like), and Γ_7^- (*s*-like) conduction bands.¹⁷ The use of a 14-band Hamiltonian is justified by the fact that the matrix elements E_p and E_{px} between the valence bands and the *s*-like and *p*-like conduction bands are of the same order of magnitude in Si or Si_{1-x}Ge_x alloys and because the *p*-like conduction band is lower in energy than the *s*-like conduction band.¹⁸ The parameters used in the calculation are re-

TABLE I. Parameters used in the 14-band structure calculation. $\tilde{\gamma}_1$, $\tilde{\gamma}_2$, and $\tilde{\gamma}_3$ are the Luttinger-like parameters. E_p and E_{px} are the optical matrix elements, E_g is the energy gap, and E_{gc} is the offset between Γ_7 and Γ_8 . Δ and Δ_c are the spin-orbit couplings of the valence band and the conduction band (after Refs. 7 and 17).

	$\tilde{\gamma}_1$	$\tilde{\gamma}_2$	$\tilde{\gamma}_3$	E_p (eV)	E_{px} (eV)	E_g (eV)	E_{gc} (eV)	Δ (meV)	Δ_c (eV)
Si	-0.64	0.076	-0.283	25	15	4.185	-0.775	44	0
Si _{0.5} Ge _{0.5}	-0.398	0.026	-0.4	25	15	2.54	0.725	170	0.093

ported in Table I. The influence of the remote bands on the valence-band states is taken into account by the $\tilde{\gamma}_i$ Luttinger-like parameters. The parameters $\tilde{\gamma}_c$ introduced in Ref. 17 are taken to be equal to zero. The $\tilde{\gamma}_c$ parameters do not couple directly the conduction band to the valence bands. The change of parabolicity of the conduction band induced by the remote bands can be neglected as compared to the energy difference between the conduction band and the valence band near the Γ point. The effect of the first p -like and s -like bands on the valence band is thus very weakly affected by taking $\tilde{\gamma}_c=0$. We have chosen to model the optical properties of the islands with a two-dimensional 14-band formalism instead of a three-dimensional calculation in the effective mass approximation.¹⁹ This choice is justified by the island height and by the fact that we want to calculate the matrix elements of the intraband optical transitions taking into account the band mixing. The average composition of the islands was taken to be equal to 50% Ge, as deduced by electron-diffraction measurements on single islands.³ As the germanium content and composition profile are not known exactly for these structures, a biaxial strain equivalent to that of a two-dimensional layer was considered.³ We have neglected in the calculation the strain variation within the islands and the vertical inhomogeneity in the island stack. The partial strain-induced deformation of the silicon surrounding the islands has also been neglected. The parameters used for the strained Hamiltonian can be found in Ref. 20. A 350-meV heavy-hole valence-band offset for a strained Si_{0.5}Ge_{0.5} layer on silicon is assumed.^{7,20} The islands are approximated as 20-nm-thick SiGe layers deposited on a 1.3-nm-thick SiGe 50% layer representing the wetting layer. A three-dimensional calculation of the electronic structure shows that the confined states in the islands become delocalized in the wetting layer for energies just beneath the energy of the first confined subband of the wetting layer.¹⁹ The wave function of these states become “quantum-well-like” for energies close to the wetting layer subband. It is thus legitimate to approximate this continuum of states by the subband of the two-dimensional wetting layer. Note that midinfrared spatially direct optical transitions between quantum dot ground states to two-dimensional wetting layer states have been experimentally evidenced in Refs. 21 and 22. The electronic spectrum of the wetting layer is calculated independently of the electronic spectrum of the islands. The intersubband dipole matrix elements are obtained within the 14-band $\mathbf{k}\cdot\mathbf{p}$ formalism in the dipolar approximation and using the calculated wave functions for the islands and the wetting layer. The calculation principle of the dipole matrix elements is given in the Appendix. A detailed comparison between the 14-band and the 6-band $\mathbf{k}\cdot\mathbf{p}$ formalism which only describes

the valence band can be found in Ref. 23. It is, in particular, shown that a 6-band calculation can overestimate by a factor of 2 the amplitude of the intersubband absorption.

Figure 5(a) shows the in-plane subband dispersion diagram along the [110] direction for the 1.3-nm-thick wetting layer and for the 20-nm-thick SiGe layer [Fig. 5(b)]. The origin of energy is taken at the silicon heavy-hole valence-band edge. Only the first confined subbands are reported in the diagram. In the case of the wetting layer, only two subbands, the heavy-hole HH₁, and the light-hole LH₁, are confined. The heavy-hole subband is found at 163 meV from the band edge, in agreement with photoluminescence measurements. The energy splitting between HH₁ and LH₁ is 63 meV. The number of confined states is much larger for the large well, i.e., in the islands. Thicknesses of 20 and 1.3 nm lead to an energy difference of 185 meV between the heavy-hole subband HH₁ of the large well and the heavy-hole subband of the small well, which corresponds closely to the energy difference experimentally observed. Figure 6 shows a schematic diagram of the potential structure along the z growth axis for the wetting layer and the SiGe island.

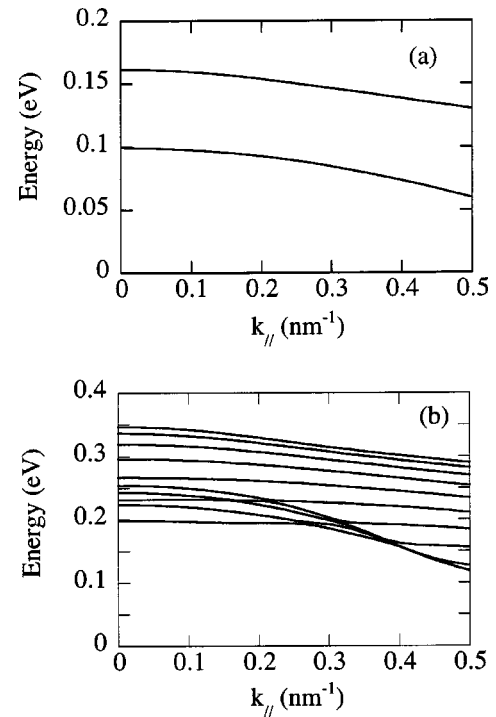


FIG. 5. (a) In-plane valence dispersion diagram along the [110] direction for a 1.3-nm-thick Si_{0.5}Ge_{0.5} quantum well. The z growth axis is along the [001] direction. The origin of energy is taken at the heavy-hole band edge of silicon. (b) In-plane dispersion diagram along the [110] direction for a 20-nm-thick Si_{0.5}Ge_{0.5} quantum well. Only the first confined subbands are reported.

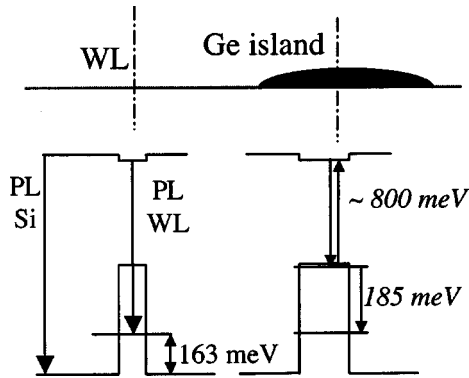


FIG. 6. Schematic (not to scale) heterostructure potential profile along the growth axis as obtained through the wetting layer and through the GeSi island. The low-temperature band gap of compressively strained $\text{Si}_{0.5}\text{Ge}_{0.5}$ is calculated at 780 meV. The energies of the experimentally observed transitions and the corresponding energy levels are indicated in italic.

The calculated spectral dependence of the absorption in TM polarization is shown in Fig. 7. The calculation was performed for a two-dimensional carrier density of $7 \times 10^{10} \text{ cm}^{-2}$. In the midinfrared above 100 meV, the absorption is dominated by a resonance around 185 meV which is strongly TM polarized. This transition corresponds to a spatially direct transition. In TM polarization, an additional resonance is observed at 120 meV, along with much stronger resonances at lower energy. Figure 7 also shows a comparison between the transverse-electric (TE)-polarized and the TM-polarized absorption spectra. As experimentally observed, the TE-polarized absorption does not exhibit any resonance around 200 meV. The broadening of the calculated absorption is 40 meV and mainly results from the value of homogeneous broadening introduced in the calculation. The inhomogeneous broadening of the dots induced by the size and the composition fluctuations is not taken into account. The comparison between the calculation and the experimental electroabsorption spectra shows that the intraband absorption properties of the islands are correctly described by using the quantum well approximation.

Figure 8 shows the dependence of the dipole matrix element for the absorption at 185 meV for TM and TE polarizations as a function of the in-plane wave vector. At the center of the Brillouin zone, the dipole matrix element is along the z direction. As the wave vector increases, a TE-polarized component is observed. However, the absorption

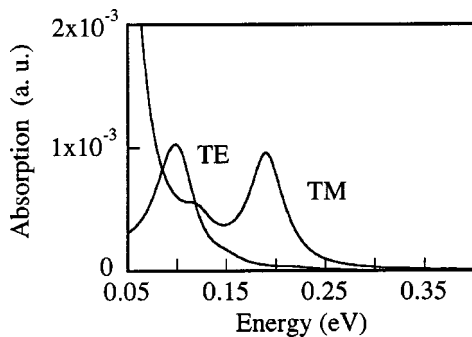


FIG. 7. Calculated spectral dependence of the intraband absorption in TM and TE polarizations. The two-dimensional carrier density is $7 \times 10^{10} \text{ cm}^{-2}$.

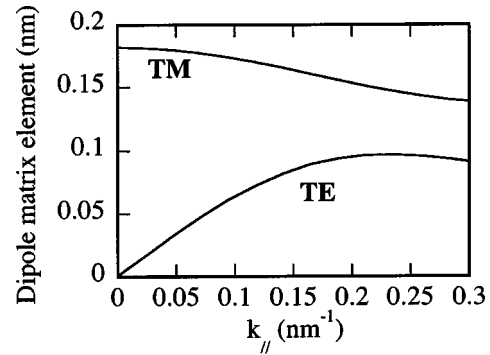


FIG. 8. Dipole matrix element as a function of the in-plane wave vector for the 185-meV resonance for TM and TE orientations.

remains strongly TM polarized even at large carrier densities, as experimentally observed. At room temperature, a wave vector $k_{||}=0.1 \text{ nm}^{-1}$ corresponds to a bidimensional carrier density of $7.6 \times 10^{11} \text{ cm}^{-2}$.

V. CARRIER DENSITY AND RECOMBINATION KINETICS

As shown in Fig. 8, the dipole matrix elements associated with the intersubband transitions were obtained from the calculation. At low carrier densities, the absorption can be described by the product of the carrier density times the absorption cross section. An absorption cross section $\sigma=7 \times 10^{-17} \text{ cm}^2$ is deduced for the resonance at 185 meV from the calculation of the matrix elements. The hole population of the islands under forward bias can thus be deduced from the amplitude of the electroabsorption. Figure 9 shows the dependence of the electroabsorption modulation as a function of the injected current density. A sublinear dependence is observed for the modulation amplitude. It indicates that the carrier density trapped in the islands saturates as the current density increases. A similar saturation was already reported in current-induced intersubband absorption in GaAs/GaAlAs quantum wells.²⁴ The bound-to-continuum intersubband modulation amplitude at resonance is proportional to the absorption cross section as calculated with the 14-band $\mathbf{k} \cdot \mathbf{p}$ formalism times the carrier density, the waveguide length, and the overlap factor between the island layers and the propagating mode. In TM polarization and at 2.5- μm wavelength, a factor of 1.5×10^{-4} was estimated for the overlap of

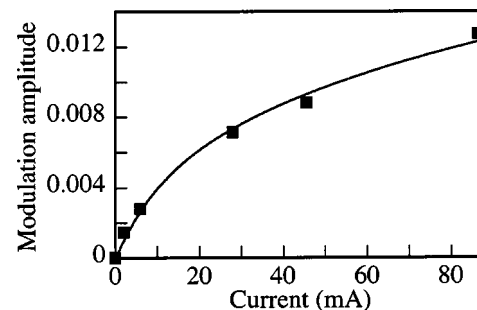


FIG. 9. Dependence of the current-induced absorption amplitude of 185 meV measured in TM polarization as a function of the injected current. The full line is a numerical fit obtained with Eq. (1).

the first confined optical mode and the island layers. In the following, we have used this value to calculate the carrier density trapped in the islands.

At room temperature, the estimation of the carrier concentration n trapped in the islands accounts for the injected carrier density for the nonradiative recombination mechanisms which are proportional to n and for the radiative recombination proportional to n^2 . Nonradiative band-to-band Auger-related recombination mechanisms are proportional to n^3 and involve either electron–electron–hole processes or electron–hole–hole processes. The carrier density trapped in the islands is given under a steady-state regime and high injection levels by Eq. (1).²⁵

$$\frac{I}{eSd} = An + Bn^2 + Cn^3, \quad (1)$$

where I is the injected current, e the electronic charge, S the area of the device cross section, and d the thickness where the carrier recombination occurs. A is an extrinsic parameter and corresponds to the monomolecular recombination coefficient while B corresponds to the bimolecular recombination coefficient. B is an intrinsic parameter characteristic of the radiative recombination in these indirect band-gap semiconductors. The value of $B(2 \times 10^{-14} \text{ cm}^3 \text{ s}^{-1})$ was deduced from the calculated recombination rate in Ge.²⁶ Equation (1) assumes that the recombination dynamics is governed by the carrier trapping in the islands and that the number of injected carriers in the islands is given by the current density. It does not account for the transfer of carriers between the barriers and the islands. We note that at room temperature only the radiative recombination in the islands is observed by electroluminescence. We emphasize that Eq. (1) assumes a uniform distribution of the carriers within the Ge layers and that the main source of recombination occurs in the islands, i.e., not in other regions outside the multiple layers of islands. The estimation of the Auger recombination coefficient as described below is dependent on this assumption.

We have fitted the island carrier density deduced from the intraband absorption following Eq. (1) by varying parameters A and C . We note that a satisfying agreement cannot be obtained without accounting for the Auger mechanism. Without this term, a bimolecular recombination coefficient more than two orders of magnitude larger than the theoretical value would be obtained. At high injected current densities, an equivalent three-dimensional carrier density in the island layers is $3 \times 10^{18} \text{ cm}^{-3}$. A monomolecular recombination coefficient $A^{-1} \sim 0.2 \mu\text{s}$ is obtained from the measurements in the low-excitation regime. An Auger recombination coefficient $C = 1.6 \times 10^{-30} \text{ cm}^6 \text{ s}^{-1}$ is deduced from the numerical fitting at high excitation densities. The radiative recombination in the islands has only a weak contribution as compared to Auger processes. The Auger recombination coefficient associated with the islands has to be compared with the values reported in silicon. At room temperature, Auger coefficients in the range of $(1-3) \times 10^{-31} \text{ cm}^6 \text{ s}^{-1}$ were measured in highly doped and highly excited silicon.²⁷ Hangleiter and Häcker have shown by a quantitative calculation that electron–hole correlations lead to an enhancement of band-to-band Auger recombination.²⁸ This enhanced Auger recom-

bination is even more pronounced at low carrier densities with an enhancement factor reaching a factor of 30 at room temperature in silicon. In self-assembled islands, one expects the carrier localization to lead to enhanced Coulomb correlations. The Auger recombination coefficient $C = 1.6 \times 10^{-30} \text{ cm}^6 \text{ s}^{-1}$ in the islands indicates an enhancement of the Auger coefficient as compared to the value reported for bulk silicon at high excitation densities. This value is also larger than the Auger recombination parameter ($8 \times 10^{-31} \text{ cm}^6 \text{ s}^{-1}$) estimated from electroluminescence spectra of $\text{Si}_{0.8}\text{Ge}_{0.2}$ layers.²⁹ We note that these parameters give also a satisfying agreement for the dependence of the modulation amplitude in the near infrared as a function of the current density. The midinfrared measurements thus provides an indirect measurement of the carrier dynamics at room temperature in the self-assembled islands.

VI. CONCLUSION

In conclusion, we have simultaneously investigated the interband and the intraband absorption properties of Ge/Si self-assembled islands under current injection. The carrier trapping in the islands leads to a bleaching of the interband absorption and to an intraband absorption between the island's lowest lying states and the wetting layer ground subband. The carrier filling and the island hole population were monitored by the amplitude of the intraband absorption. The assignment of the optical transitions was supported by a 14-band quantum well $\mathbf{k} \cdot \mathbf{p}$ calculation. The z -polarized high-energy intraband absorption was attributed to a transition from the island ground state to the two-dimensional wetting layer states. We have shown that the filling of the islands is limited at high current injection by an Auger-related mechanism. At room temperature, an Auger recombination coefficient in the islands, $C = 1.6 \times 10^{-30} \text{ cm}^6 \text{ s}^{-1}$, was deduced from the midinfrared absorption modulation amplitude.

ACKNOWLEDGMENT

This work was partly supported by the Réseau Micro et Nanotechnologie (RMNT) under Contract No. 00V0091.

APPENDIX: DIPOLE MATRIX ELEMENTS

The wetting layer and the islands are approximated by quantum wells with thicknesses along the z direction of 1.3 and 5 nm, respectively. The origin of the lower potential barrier of both quantum wells is taken at $z=0$. The calculation of the dipolar matrix element is obtained as follows. The momentum matrix element between an initial i state and a final f state is given by the expression²³

$$(\boldsymbol{\epsilon}\mathbf{P})_{i,f} = \left(\frac{m_0}{\hbar} \right) \left\langle \boldsymbol{\epsilon} \frac{\partial H_k}{\partial \mathbf{k}} \right\rangle_{i,f}, \quad (\text{A1})$$

where $\boldsymbol{\epsilon}$ is a unit vector parallel to the light polarization. As the dipole operator is related to the momentum operator, the dipolar matrix element is given for an in-plane wavevector k_{\parallel} by

$$(\boldsymbol{\varepsilon}\boldsymbol{\mu})_{i,f}^{k_{\parallel}} = \frac{e \left\langle \boldsymbol{\varepsilon} \frac{\partial H_k}{\partial \mathbf{k}} \right\rangle_{i,f}^{k_{\parallel}}}{\hbar \omega_{i,f}^{k_{\parallel}}}. \quad (\text{A2})$$

The term $\hbar \omega_{i,f}^{k_{\parallel}}$ is the energy difference between the initial and the final state. The computation of the dipole $(\boldsymbol{\varepsilon}\boldsymbol{\mu})_{i,f}^{k_{\parallel}}$ is made by using the scalar product $\boldsymbol{\varepsilon} \nabla_{\mathbf{k}} H_k$. The details of the projection of the matrix on the 14-band basis can be found in Ref. 23.

¹D. J. Eaglesham and M. Cerullo, Phys. Rev. Lett. **64**, 1943 (1990).

²J. Drucker, IEEE J. Quantum Electron. **38**, 975 (2002).

³G. Patriarache, I. Sagnes, P. Boucaud, V. Le Thanh, D. Bouchier, C. Hernandez, Y. Campidelli, and D. Bensahel, Appl. Phys. Lett. **77**, 370 (2000).

⁴A. Hesse, J. Stangl, V. Holy, T. Roch, G. Bauer, O. G. Schmidt, U. Denker, and B. Struth, Phys. Rev. B **66**, 085321 (2002).

⁵G. Abstreiter, P. Schittenhelm, C. Engel, E. Silveira, A. Zrenner, D. Meertens, and W. Jäger, Semicond. Sci. Technol. **11**, 1521 (1996).

⁶C. G. Van de Walle and R. M. Martin, Phys. Rev. B **34**, 5621 (1986).

⁷T. Fromherz, E. Koppensteiner, M. Helm, G. Bauer, J. F. Nützel, and G. Abstreiter, Phys. Rev. B **50**, 15073 (1994).

⁸J. Oiknine-Schlesinger, M. Gerling, D. Gershoni, E. Ehrenfreund, and D. Ritter, Phys. Rev. B **61**, 10972 (2000).

⁹A. I. Yakimov, N. P. Stepina, A. V. Dvurechenskii, A. I. Nikiforov, and A. V. Nenashev, Phys. Rev. B **63**, 045312 (2001).

¹⁰M. El kurdi, P. Boucaud, S. Sauvage, O. Kermarrec, Y. Campidelli, D. Bensahel, G. Saint-Girons, and I. Sagnes, Appl. Phys. Lett. **80**, 509 (2002).

¹¹B. Schüppert, J. Schmidtchen, A. Splett, U. Fischer, T. Zinke, R. Moosburger, and K. Pettermann, J. Lightwave Technol. **14**, 2311 (1996).

¹²M. El kurdi *et al.*, Physica E (Amsterdam) **16**, 450 (2003).

¹³P. Sutter, E. Mateeva-Sutter, and L. Vescan, Appl. Phys. Lett. **78**, 1736 (2001).

¹⁴M. De Seta, G. Capellini, F. Evangelisti, and C. Spinella, J. Appl. Phys. **92**, 614 (2002).

¹⁵S. A. Chaparro, J. Drucker, Y. Zhang, D. Chandrasekhar, M. R. McCartney, and D. J. Smith, Phys. Rev. Lett. **83**, 1199 (1999).

¹⁶O. G. Schmidt, K. Eberl, and Y. Rau, Phys. Rev. B **62**, 16715 (2000).

¹⁷S. Ridene, K. Boujdaria, H. Bouchriha, and G. Fishman, Phys. Rev. B **64**, 085329 (2001).

¹⁸P. Pfeffer and W. Zawadzki, Phys. Rev. B **41**, 1561 (1990).

¹⁹P. Boucaud *et al.*, Phys. Rev. B **64**, 155310 (2001).

²⁰M. M. Rieger and P. Vogl, Phys. Rev. B **48**, 14276 (1993).

²¹S. Sauvage, P. Boucaud, F. H. Julien, J.-M. Gérard, and V. Thierry-Mieg, Appl. Phys. Lett. **71**, 2785 (1997).

²²S. Sauvage, P. Boucaud, J.-M. Gérard, and V. Thierry-Mieg, Phys. Rev. B **58**, 10562 (1998).

²³M. El kurdi, G. Fishman, S. Sauvage, and P. Boucaud, Phys. Rev. B **68**, 165333 (2003).

²⁴A. Fenigstein, A. Fraenkel, E. Finkman, G. Bahir, and S. E. Schacham, Appl. Phys. Lett. **66**, 2513 (1995).

²⁵S. L. Chuang, *Physics of Optoelectronic Devices* (Wiley Interscience, New York, 1995).

²⁶W. Van Roosbroeck and W. Shockley, Phys. Rev. **94**, 1558 (1954).

²⁷J. Dziewior and W. Schmid, Appl. Phys. Lett. **31**, 346 (1977).

²⁸A. Hangleiter and R. Häcker, Phys. Rev. Lett. **65**, 215 (1990).

²⁹T. Stoica and L. Vescan, *ICSI3*, Proceedings of the SiGe Conference, Santa Fe, NM, March 2003, p. 258.